Geothermics 104 (2022) 102466

Contents lists available at ScienceDirect

Geothermics

journal homepage: www.elsevier.com/locate/geothermics

Modelling of cohesive expandable LCMs for fractures with large apertures

Lu Lee [a], Musaab Magzoub [b], Arash Dahi Taleghani [a,*], Saeed Salehi [b], Guoqiang Li [c]

[a] Penn State University, PA, United States
[b] University of Oklahoma, OK, United States
[c] Louisiana State University, LA, United States

ARTICLE INFO

Keywords:
Lost circulation
Fracture sealing
Shape memory polymer
Discrete element methods

ABSTRACT

The problem of loss circulation in geothermal wells is inherently challenging due to high temperatures, brittle rocks, and presence of abundant fractures. Because of the inherent challenges in geothermal environments, there are limitations in selecting proper lost circulation materials (LCMs). Traditional LCMs such as calcium carbonates that are commonly used in the oil and gas drilling may be softened and prone to failure during geothermal drilling. Moreover, evaluating the performance of different LCMs for geothermal drilling requires unique testing setups, which is expensive, and complicated to run due to harsh environmental conditions of geothermal systems. Herein, we present a numerical approach to simulate LCM transport and bridging through fractures in downhole conditions. By discrete element methods, each individual particle trajectory, and their interactions with the fluid and surrounding particles are incorporated into the analysis. To validate the model, we used experimental results acquired from a high-temperature flow loop system built specifically for this purpose. We took a further step in this work and considered LCM particles that are made from a shape memory polymer (SMP). These particles start expanding and adhering to each other in downhole conditions. The use of SMP is shown to be advantageous in sealing large fractures (3 mm aperture). We demonstrated how numerical modelling may supplement laboratory tests to show initiation of the bridging process, fracture plugging or even its failure. Using the proposed methodology may significantly reduce the number of experiments needed to find an effective LCM recipe, hence drillers can save time and costs by assessing different LCM systems numerically.

1. Introduction

Lost circulation could be a troublesome event that often occurs during drilling operations especially in brittle rocks. Excessive amount of drilling fluid is lost into the formation matrix through large pore openings or fracture networks. In this work, we focus on fluid loss through fractures as it poses more challenges while drilling crystalline geothermal systems. The loss severity is generally classified into four types, seepage loss (less than 10 bbl/hr), partial loss (10 to 100 bbl/hr), severe loss (100 to 500 bbl/hr), and total loss (more than 500 bbl/hr) (Barret et al., 1990; Alsaba et al., 2014). Depending on its severity, the consequences of a lost circulation event may vary from just an additional cost and formation damage to well control problems. A fluid loss event not only puts the operation at risk but also jeopardizes the safety of the field personnel. Rigorous well design and planning should be in place to anticipate any possible lost circulation situations given that the impact is certainly negative.

Various techniques such as managed pressure drilling, casing while drilling, and cement plugging are employed to prevent severe fluid loss. Managed pressure drilling is an adaptive technique to control the annular pressure. Casing while drilling prevents the direct exposure of formations while drilling and eliminates the classic casing runs. While the managed pressure drilling and casing while drilling techniques are very effective at the cost of extra financial incurrence in oil and gas wells, but the counterpart technologies are not yet adopted to geothermal conditions. On the other hand, cement plugging is frequently used as the last resort to minimize fluid loss and regain returns at the surface in geothermal drilling.

The LCMs usually work very well in formations with naturally and induced fractures as long as fracture apertures are not too large or are less than 2 mm (Lavrov, 2016). These LCMs are the conventional granular, fibrous, and flaky materials defined by their shapes and functions in sealing fractures (Alsaba et al., 2014). Granular LCMs are often the most basic additives. For example, calcium carbonate has been heavily utilized both in the laboratory and field settings (Wang et al., 2019). Other granular additives such as graphite and gilsonite are some

* Corresponding author at: Department of Energy and Mineral Engineering, University Park, PA 16802, United States
E-mail address: arash.dahi@psu.edu (A. Dahi Taleghani).

https://doi.org/10.1016/j.geothermics.2022.102466
Received 1 October 2021; Received in revised form 5 May 2022; Accepted 16 May 2022
Available online 25 May 2022

of other alternative options in sealing fractures (Razavi et al., 2015). These granular particles exhibit superior ability in bridging fractures. Once inside the fracture, the granular particulates settle, accumulate, and stack on one another to bridge across the permeable channel. The fibrous and flaky materials, on the other hand, supplement the granular particles in sealing fractures. They are more often mixed with the granular LCMs to enhance the bridging process and form a seal by filling the gap between the granular particles. Conventional LCMs have serious size limitations due to the constraints of the downhole equipment. While the LCMs are capable of sealing off fractures to a certain size, the bottomhole assembly can at the same time be damaged. Increasing both particle size and concentration may be one strategy in combating severe fluid loss. However, this usually becomes an issue because of the limited clearance of bottomhole assembly, which may further require using a circulating sub or tripping out of the hole.

It would be very difficult to stop fluid loss with conventional LCMs on large fractures, not to mention that the loss is more intensified in geothermal settings. Compared to the conventional oil and gas reservoirs, geothermal reservoirs typically exhibit themselves with underpressurized, hard, and highly fractured formations (Finger and Blankenship, 2012). There can easily be a notable overbalance drilling without using a lightweight fluid. In addition, the highly fractured formation makes it even more challenging to prevent and stop the loss. It is not atypical to encounter fracture apertures in excess of 5 mm in geothermal surroundings (Lavrov, 2016). In order to solve the shortcoming of sealing large fractures, LCMs made of shape memory polymers (SMP) have emerged (Mansour et al., 2018; Magzoub et al., 2021). The SMP exhibit the ability to recover its original state from the temporarily deformed shape when triggered by external stimuli such as heat, pH, light, etc. (Li, 2014). The SMP may come in different shapes, from simple granular to more sophisticated geometries such as spirals and spider nets, which have been developed recently (Tabatabaei and Dahi Taleghani, 2021; Tabatabaei et al., 2021). Here, we have only considered the SMP as simple granular geometries in both the numerical simulations and laboratory tests. The SMP has been widely used in sealing applications where there are structural damages. In a similar situation, one may take advantage of the SMP to overcome the size limitation of bottomhole assembly for fracture sealing.

Successful fracture sealing can be attributed from many factors including both fluid properties and the LCMs mixed within it. The main functions of a drilling fluid are to lubricate the drilling string, remove cuttings, and at the same time, to minimize formation damages. For the application of lost circulation prevention, drilling fluid is the medium that transports LCMs into the pores and fractures. Its rheology plays an important role in maintaining the pressure balance between the wellbore and surrounding formations. This is even more important in a geothermal environment since the fluid properties, such as yield stress and plastic viscosity, can be drastically altered when reaching a failure temperature (Amani et al., 2012; Galindo et al., 2015; Avci and Mert, 2019). Table 1 shows the viscosity variation of different drilling fluids under various temperature settings. Although oil-based mud is more resilient than water-based mud in high-pressure and high-temperature wells because of its thermal stability, oil-based mud has not been commercialized in geothermal drilling applications, and we will only consider the water-based mud in this research.

Table 1
Fluid property measurements in different temperature ranges.

Fluid Type	Temperature (°C)	Plastic Viscosity (mPa•s)	Yield Point (Pa)	Reference
Oil-Based	38 to 260	52.5 to 40	85 to 10	Amani et al. (2012)
Water-Based	38 to 260	4.25 to 0.49	2.5 to -0.08	
	50 to 200	29.3 to 12.7	18.4 to 5.0	Galindo et al. (2015)
	15 to 150	10.7 to 2.3	9.2 to -0.41	Avci and Mert (2019)

When it comes to the LCMs, the particle size distribution (PSD) is one major factor in effective fracture sealing besides their classified shapes. The importance of the PSD in fracture sealing applications began gaining attention in the early days (Gatlin and Nemir, 1961). Most of the PSD design guidelines are based on laboratory results and field empirical formula (Abrams, 1977; Vickers et al., 2006; Alsaba et al., 2017). Some PSD design considerations presume the optimal packing geometry of granular materials by supposing a well-rounded spherical particles (Dick et al., 2000; Chellappah and Aston, 2012). While it is still an ongoing research topic, the PSD that is currently utilized for many field applications contains bimodal or even multimodal PSD of LCMs for effective sealing (*e.g.* Whitfill et al., 2011). The sealing capability of bimodally distributed LCMs has been verified in the laboratory experiments and numerical simulations (Razavi et al., 2016; Lee and Dahi Taleghani, 2020). This paper is to explore the capabilities of developing a numerical model that can help assist laboratory results.

2. Material and Methods

In this section, the numerical model and the experimental setup are described in detail. The purpose of the paper is to study the applicability of fracture sealing (aperture of 3 mm) by the SMP mixed with water-based mud. If successful, this numerical model can be employed to supplement laboratory test results and also to save high costs of laboratory works.

2.1. *Coupled CFD-DEM Simulation*

Fracture sealing applications involve small particulates, often granular, to flow into a narrow channel. Currently existing numerical modeling techniques include the continuum and the discrete approaches. For the continuum approach, it is described by mass and momentum conservation equations with initial and boundary conditions (Gidaspow, 1994). This can be applied to both the solid (particles) and fluid (water) phase on a macro-scale. For example, the two-fluid model that belongs to the continuum approach treats both solid and fluid as two fluid-like interpenetrating media in computational grid cells (Anderson and Jackson, 1967). Since the solid phase is treated as a fluid-like phase, parameters such as pressure and viscosity are necessary to describe the cluster of particles. This may be very effective in solving flow with a very large number of particles since the computational consumption can be less taxing than the discrete method. However, it may not be accurate in describing particle-scale scenarios such as fracture sealing. On the other hand, the discrete approach or the discrete element method (DEM) focuses on the individual particle's motion analysis influenced by other particles' contact and non-contact forces (Cundall and Strack, 1979). Particles are described in a microscopic level. Since each particle is treated discretely apart from each other, Newton's law of motion can be applied to describe the location and velocity of individual particles without the need of grid cells.

The combined techniques of computational fluid dynamics (CFD) and DEM, also known as the coupled CFD-DEM, is a continuum-discrete approach where the CFD solves the fluid flow by Navier-Stokes equations for each locally averaged cell while the DEM controls the particulate phase. The CFD-DEM can be employed to accurately capture particle trajectory especially in the application of fracture sealing where particle settlement and accumulation take place inside a permeable path. In addition, the micro-scale model from the DEM can be mapped onto the macro-scale grid cells through the particle-fluid interactions (Zhou et al., 2010). The CFD-DEM is a very suitable numerical simulation tool to apply on fracture sealing situation in laboratory settings. Therefore, we will be adopting the coupled CFD-DEM approach to simulate the particulate flow and investigate the fracture bridging and sealing phenomenon.

The governing equations of the DEM follow simple Newton's law of motion. For every particle, the translational force balance is described as

$$m_i\frac{d\nu_i}{dt} = m_i g + \sum_{j=1}^{c}\left(f_{n,\ ij} + f_{t,\ ij}\right) + f_{pf,\ i}, \tag{1}$$

Particle interactions are treated in pairs where particle i may be in close contact with another particle j. Equation (1) describes the linear motion that includes gravitational force, both normal $f_{n,\ ij}$ and tangential forces $f_{t,\ ij}$, and particle-fluid interaction force $f_{pf,\ i}$. The normal and tangential forces can be rewritten as

$$f_{n,\ ij} = k_n\delta_{n,\ ij} - \gamma_n\nu_{n,\ ij} + f_{c,\ ij}, \tag{2}$$

and

$$f_{t,\ ij} = k_t\delta_{t,\ ij} - \gamma_t\nu_{t,\ ij}. \tag{3}$$

The three terms in Equation (2) describe spring, damping, and cohesive forces while the two terms in Equation (3) describe the shear and damping forces. These two equations use the simple linear spring-dashpot model as depicted in Figure 1 (Kloss et al., 2012). When particles are in contact, the program allows slight overlaps to represent elastic deformation. For spring force, $\delta_{n,\ ij}$ is the overlap distance between the two particles in contact measured from their spherical center. On the other hand, $\delta_{t,\ ij}$ is the tangential displacement between two particles. The tangential contact force is also limited to be as

$$f_{t,\ ij} = \mu_{i,\ j} f_{n,\ ij}. \tag{4}$$

Equation (4) is the Coulomb friction limit so that the tangential contact force is a linear portion of the normal contact force, where friction coefficient, $\mu_{i,\ j}$, is between 0 and 1. The coefficients k_n and k_t are elastic constant for normal and tangential contact while γ_n and γ_t are viscoelastic damping constant for normal and tangential contact. These can be determined based on the Hertzian contact model (Hertz, 1882).

In addition to the classic Hertzian contact model, particles may also agglomerate to form large clusters. The agglomeration is due to the cohesive nature of the material that attracts one another during surface contacts, especially for polymers. The mechanisms behind polymer cohesion can be attributed to mechanical, chemical, electrical, diffusion, and more (Fourche, 1995). The overall cohesive force can be described by imposing one additional force to maintain contact. A simplified Johnson-Kendall-Roberts (JKR) model is considered in the simulation to describe the contact forces developing between colliding particles (Johnson et al., 1971). The cohesive force can be described as

$$f_{c,\ ij} = kA, \tag{5}$$

and

$$A = \frac{\pi\left(l - r_i - r_j\right)\left(l + r_i - r_j\right)\left(l - r_i + r_j\right)\left(l + r_i + r_j\right)}{4l^2}, \tag{6}$$

where k is the cohesion energy density that can be calibrated both experimentally and numerically (Roessler and Katterfeld, 2019). A is the particle contact area, l is the distance between particle centers, and r_i and r_j are the radius of the two touching particles. We presumed that the surrounding fluid has no explicit impact on particles' agglomeration other than the heat transfer.

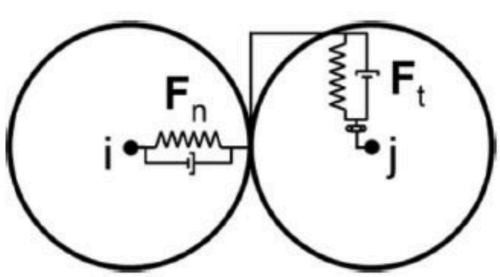

Fig. 1. The linear spring-dashpot model (Kloss et al., 2012).

The particle-fluid interaction force, $f_{pf,\ i}$, is a key force for the DEM to communicate with the CFD algorithm. Without the interaction force with fluid, the particles move as if they exist in vacuum. The particle-fluid interaction consists of many forces that include drag force, pressure gradient force, viscous force, virtual mass force, Basset force, list force, and Magnus force (Saffman, 1964; Candelier et al., 2004; Maruyama, 2011). All the interaction forces with the surrounding fluids are averaged when particles are mapped onto their respective cell grids by the CFD algorithm. With averaging, non-dominant forces can be considered negligible. We then only consider the dominant forces, which include the pressure gradient, viscous, and drag forces. Therefore, the particle-fluid interaction is written as

$$f_{pf,\ i} = f_{\nabla p,\ i} + f_{\nabla\cdot\tau,\ i} + f_{d,\ i}, \tag{7}$$

where $f_{\nabla p,\ i}$ and $f_{\nabla\cdot\tau,\ i}$ are the pressure gradient force and viscous force, respectively.

The Di Felice (1994) drag model is implemented here due to its accuracy with the experimental terminal velocity of a wide range of Reynolds numbers as well as the consideration of the effect from surrounding particles. The fluid drag force exerted on particles is described as

$$f_{d,\ i} = \frac{\pi}{8}C_{d0,\ i}\rho_f d_i^2\varepsilon_i^2\left|u_f - \nu_i\right|\left(u_f - \nu_i\right)\varepsilon_i^{-\beta}, \tag{8}$$

where

$$\begin{aligned} \mathrm{C_{d0,\ i}} &= \left(0.63 + \frac{4.8}{\sqrt{\mathrm{Re_i}}}\right)^2 \varepsilon_\mathrm{i} = 1 - \sum_{\mathrm{i=1}}^{\mathrm{n}}\frac{\mathrm{V_{p,\ i}}}{\Delta\mathrm{V}}\beta \\ &= 3.7 - 0.65\exp\left\{-\frac{\left[1.5 - \log_{10}(\mathrm{Re_i})\right]^2}{2}\right\} \end{aligned} \tag{9}$$

and

$$Re_i = \frac{\rho_f d_i \varepsilon_i\left|u_f - \nu_i\right|}{\mu_f}, \tag{10}$$

where u_f is the fluid velocity, ν_i is the particle velocity, ε_i is the void fraction, $V_{p,\ i}$ is the particle volume, and ΔV is the cell volume in CFD. This drag model is based on empirical correlations by fitting the component β for a range of Reynolds number, Re_i (Rumpf and Gupte, 1971).

For the rotational movement of particles, it follows

$$I_i\frac{d\omega_i}{dt} = \sum_{j=1}^{c}\left(M_{t,\ ij} + M_{r,\ ij}\right), \tag{11}$$

where $M_{t,\ ij}$ is the torque generated by tangential force, and $M_{r,\ ij}$ is the torque generated by the non-sphericity of particles.

It is important to note that the particles in the DEM simulation are treated as complete spheres with allowed overlapping displacement to represent the elastic deformation. Granular media rarely present themselves with complete spheres. Therefore, a non-sphericity model is needed to address such issue.

Individual particles may have various degrees of shapes. One simple method is to impose an additional torque to describe the effect of particle geometry. For example, it is easier for a very well-rounded particle to roll down a smooth ramp than an irregular shaped particle. This additional torque resulted by non-sphericity can be tuned and characterized with experimental results. Common testing technique is to obtain an angle of repose to correct the bulk particle sphericity (Goniva et al., 2012). A directional constant torque model (Ai et al., 2011) is applied.

$$M_{r,\ ij} = -\mu_r f_{n,\ ij}\left(\frac{r_i r_j}{r_i + r_j}\right)\ \frac{\omega_{\ rel}}{|\omega_{\ rel}|}, \tag{12}$$

where μ_r is the rolling friction coefficient, and $\omega_{\ rel}$ is the relative angular velocity between two particles. The motion of a fluid phase along with a secondary particulate phase is governed by the Navier-Stokes equations as (Zhou et al., 2010)

$$\frac{\partial \alpha_f}{\partial t} + \nabla\cdot\left(\alpha_f u_f\right) = 0, \tag{13}$$

and

$$\frac{\partial\left(\rho_f \alpha_f u_f\right)}{\partial t} + \nabla\cdot\left(\rho_f \alpha_f u_f u_f\right) = -\nabla p - F_{pf} + \nabla\cdot\tau + \rho_f \alpha_f g, \tag{14}$$

where

$$F_{pf} = \frac{1}{\Delta V}\sum_{i=1}^{n}\left(f_{d,\ i} + f_{\nabla p,\ i} + f_{\nabla\cdot\tau,\ i}\right). \tag{15}$$

Equations (13) and (14) are balance equations where α_f is the fluid fraction, ρ_f is the fluid density, and F_{pf} is the averaged particle-fluid interaction force in a grid cell.

2.2. Simulation Setup

The simulation geometry adopts the wellbore geometry (a cylindrical pipe intersected by an axial fracture) system with a single vertical fracture (Figure 2). This approach is to mimic the downhole drilling environment. Only one fracture is considered due to the symmetry of a typical bi-wing fracture and heavy computational consumption. The dimension of the cylindrical pipe is 25.4 by 368.3 mm (diameter by length) while the dimension of the fracture is 342.9 by 25.4 by 3 mm (length by height by width). There are two inlets and one outlet in the simulated domain. The pressure at the inlet is 400 psi maintained by a pump. One outlet at the other end of the cylindrical pipe is at 390 psi while the fracture outlet is kept at atmospheric pressure. The density of the incompressible fluid is 2,000 kg/m^3, and its viscosity follows the power law model described in subsection 3.1. The fracture is consisted of hexahedral numerical cells whose length, height, and width are 3 by 3 by 3 mm. The numerical grids of the cylindrical pipe are of both hexahedral and tetrahedral cells. The unresolved CFD-DEM algorithm requires the cell volumes larger than particle size. In addition, the Courant number is set to be below 1 to avoid numerical divergence. The DEM timestep is 10^{-7} s while the CFD timestep is 10^{-5}, and therefore, the coupling timestep is 100 DEM steps.

The LCMs are assumed to be a mixture of granular particles and SMP with 10% to 20% total concentration by volume. This mixture has Young's moduli range from 10 MPa to 100 MPa with 0.3 of Poisson's ratio. The restitution, friction coefficients are 0.5 and 0.75 for the whole system respectively. The rolling friction coefficient characterized by the solid shapes is set to be 0.75. The cohesion energy density is 1 MJ/m^3. A cohesive particle can maintain contact with another neighboring particle, increasing the chance of bridging process. The particle diameters from smallest to largest range from 0.2 mm to 2.6 mm. The rationale behind these numbers is to reduce unnecessary simulation times as well as matching the material properties in laboratory settings.

2.3. Experimental Setup

To validate the numerical model developed in this study, we used the experimental results acquired from a high-temperature flow loop. This setup is a dynamic simulator to study how drilling fluid penetrates 14" core length containing intentionally created fracture under high-pressure and high-temperature conditions. The setup consists of three main systems: the circulation system, core holding system, and filtrates collection system. The circulation system is equipped with a positive displacement pump that gives a flow rate of 2 to 4.5 gpm, which is equivalent to 3.5 ft/s to 7.7 ft/s circulation speed. The total volume inside the loop is 1,200 cm^3. The loop consists of two sections, the main loop circulates across the core to allow filtrates to pass through the fracture, and the bypass loop is used for conditioning the mud to the desired temperature. The main circulation loop is 0.488" in diameter x 160" in length. It mainly consists of a mud compensating tank, mud pump, pressure gauges, flow analyzer, and thermocouples.

The continuous fluid circulation in the flow loop simulates drilling fluid circulation inside the well while the mud tank compensates the fluid and maintains the pressure. The drilling fluid can filtrate through the fractured core while fluid loss is collected and measured. The collection system is designed to collect filtrate samples while applying backpressure to control the differential pressure across the core. Figure 3 shows the sketch of the LCM testing flow loop.

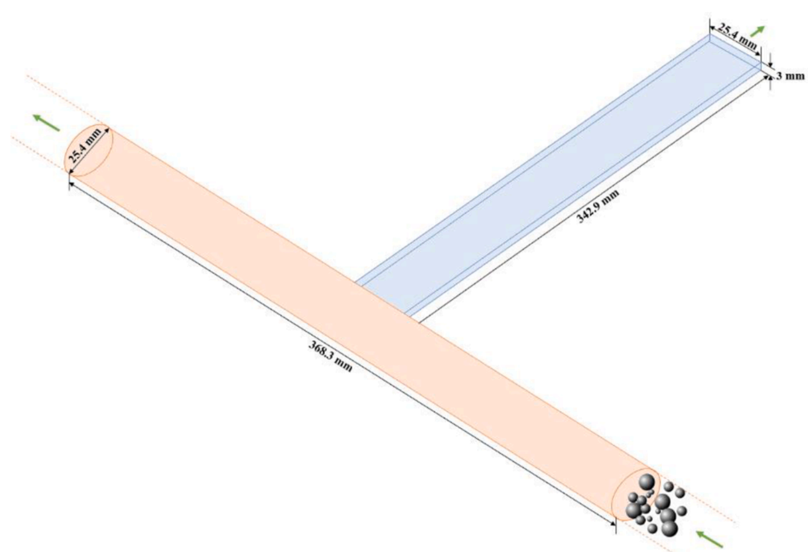

Fig. 2. A wellbore geometry system that consists of a cylindrical pipe (light brown) and a single fracture (blue). Wellbore diameter and length are 25.4 mm and 368.3 mm. Fracture length, width, and height are 342.9 mm, 3 mm, and 25.4 mm, respectively.

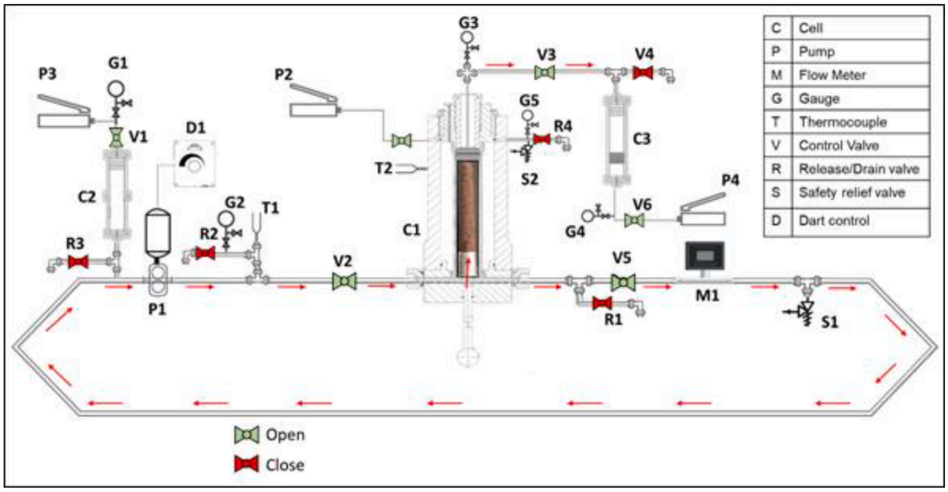

Fig. 3. **Sketch of the high-temperature dynamic LCM testing unit and a 2 × 13.5" core inserted in the confined cell (Magzoub et al., 2021).**

2.4. Rock Cores and Drilling Fluid Preparation

For the experiments conducted in the high-temperature dynamic LCM flow loop testing unit, 2 × 13.5" granite cores were used with different prefabricated fractures. Figure 4 shows the fractured core used in the LCM testing flow loop. The core was prepared from a granite rock and then cut into two pieces before welding them together with spacer and high temperature-resistant glue to make a 3,000 μm fracture, as shown in Figure 4**a**. An aluminum sheet was wrapped at the edge of the core to achieve full fitting with the core holder sleeve, as shown in Figure 4**b**. Figures 4**c** and 4**d** show the comparison of a fracture before and after the sealing experiment.

For preparing the drilling mud, a base fluid was prepared by 20 lb/bbl bentonite and 1 lb/bbl caustic soda then the different LCMs were added. Besides the SMP, two other conventional LCMs were used as a comparison, the 55 lb/bbl calcium carbonate and 5 lb/bbl cedar fiber. The calcium carbonate has wide particle size distribution with d10 = 2 μm, d50 = 15 μm, and d90 = 100 μm while cedar fiber is showing D50 of 600 μm with a wider range of particle size up to 2 mm, which is good for bridging of LCM plug. The SMP, on the other hand, has larger particles than the fiber with D50 of 1637 μm with particles ranging from 0.6 to 2.14 mm. Fiber can greatly increase the performance of LCMs in geothermal drilling, and it has high thermal stability, a wide range of particle sizes, and an aspect ratio range of 6 to 30 (Magzoub et al., 2021). The SMP used in this study was synthesized out of a commercial bisphenol A-based epoxy resin (EPON 826). The resin was cured by an isophorone diamine (IPD) crosslinker. The concentrations of the IPD and EPON 826 were set to 23.2 g and 100 g, respectively, to balance out the stoichiometry, and the thermoset network was achieved at 300 °F, which followed the previous studies by Fan and Li (2018). After that, the SMP cube samples about 1" side length was compressed to about 50% compression strain at room temperature until fracture, which completes the cold compression programming process. The fractured pieces were hammered into smaller-sized grains, ball milled to further reduce the particle sizes, and then sieved to the size explained above.

During the sealing experiments, the fluid is circulated in the flow loop until the temperature reaches the SMP activation temperature of 300 °F. The temperature activated SMP expands and achieves the sealing. The viscoelastic properties of the new shape memory polymer and mechanical properties were investigated using the dynamic mechanical analysis (DMA) tests. The results showed a high compressive strength of 320 MPa and high stiffness of 1.05 GPa at 70°F, a glass transition temperature of 300°F, and rendering high recovery stress of 17 MPa.

3. Results and Discussion

3.1. Viscosity Measurements

The viscosity measurements of the drilling fluids prepared by cedar fiber and cedar fiber/SMP mixture are presented in Figure 5. The tests

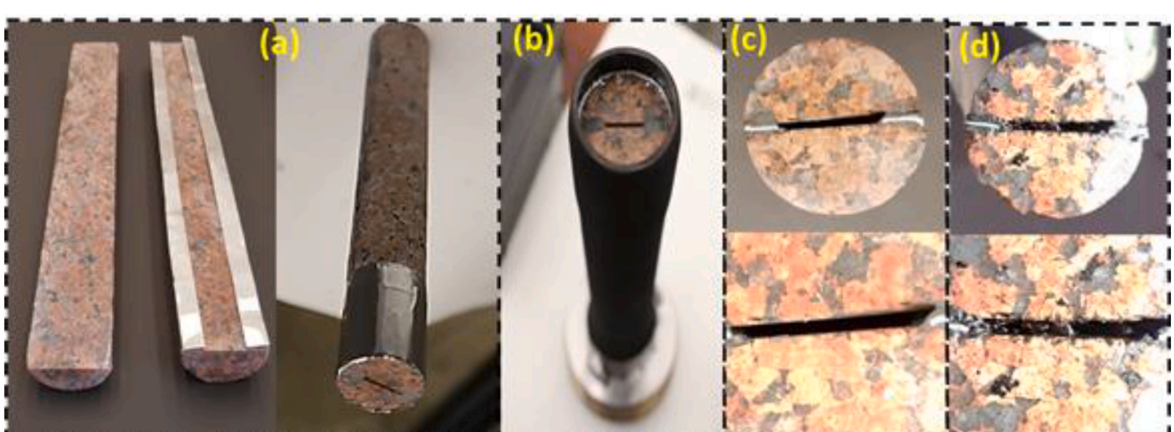

Fig. 4. A 2.5 × 13.5" core with a 3000 microns fracture, showing (a) fabrication process, (b) the sample before running the test, (c) fracture before, and (d) fracture after the sealing experiment.

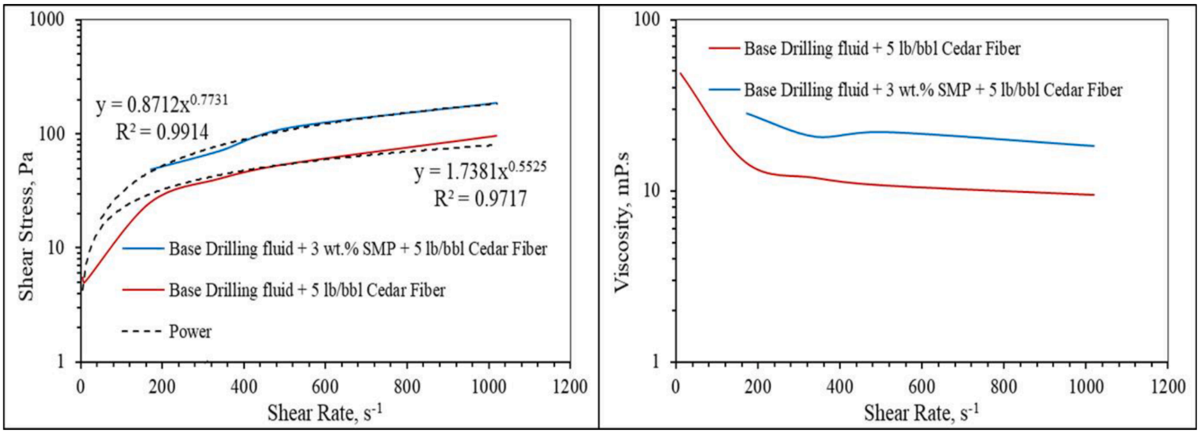

Fig. 5. Viscosity measurements of drilling fluid with cedar fiber and SMP.

were conducted using a shear rate-controlling viscometer at 200 °F. The shear rate was varied from 5 s^{-1} to 1021 s^{-1} while recording shear stress. The drilling fluid with fiber and the SMP/Fiber mixture showed a shear-thinning behavior following the power law model. The SMP increased the viscosity of the base fluid with fiber from 9 to 18 mPa.s. Moreover, the plastic viscosity and yield points were also calculated from the viscometer measurements. It showed some increase with the SMP addition by 75%. The plastic viscosity increased from 8.1 mPa.s to 14.5 mPa.s, while the yield point increased from 10.7 to 22.5 lb/100ft^2 (512 to 1060 Pa).

3.2. Sealing Experiment with the Dynamic LCM Flow Loop

The objective of this experiment is to validate the LCMs for sealing large fractures. The sealing is assessed dynamically through a circulation system meant to provide continuous fluid circulation across the core to simulate drilling fluid circulation inside the well. The tests were conducted at circulating pressures of 400 psi, maintained for 5 minutes while the fluid loss and pressure are recorded. The pressure difference between the circulating pressure and the backpressure after the fracture will be considered the sealing pressure.

Generally, LCM concentration and fracture size are the main parameters influencing the success of any mud loss treatment. This conclusion was observed in the sealing mechanism of the SMP and was reflected at the total mud loss for 5 minutes and under 400 psi circulating pressure, as presented in Figure 6. The amount of the initial SMP concentration was not enough to form a strong plug inside the 3,000 μm fracture. The solution was to increase the SMP concentration from 3 wt.% to 6 wt.% and the filtration was reduced by 88% from 70 cm^3 to 8 cm^3.

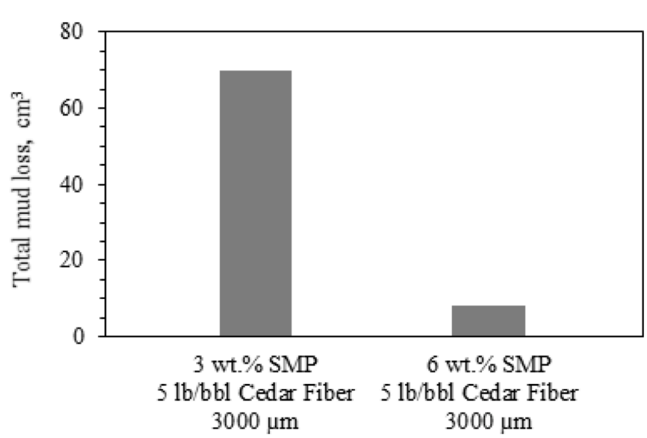

Fig. 6. Comparison of total mud loss from dynamic LCM testing experiments with different SMP concentrations.

To better examine the effect of SMP concentration on the success of the sealing treatment, the attained sealing pressure with the two different concentrations of the SMP is recorded for 5 minutes, as presented in Figure 7. The sealing pressure with the 6 wt.% SMP has mostly maintained around 400 psi which was the circulating pressure; this means that the plug formed by the SMP particles was capable of withstanding the maximum circulating pressure.

The progress of the filtration for 5 minutes is reported in Figure 8. The time-dependent mud loss was observed to be correlated to the changes in the dynamic sealing pressure. At the low concentration (3 wt.%), the SMP failed to stop the mud loss and exhibited a high loss rate during the first minute of the experiment. With the sealing completely lost after 2 minutes, the circulating pressure was lost too; this resembles the case where the well suddenly lost a huge amount of mud, and the hydrostatic pressure inside the well is lost. Later, when the mud pump was boosted to maintain the circulating pressure, the mud loss peaked again as shown in Figure 8 at 4 minutes. The case was different with the higher concentration of the SMP (6 wt.%). The mud loss was minor at a small loss rate during only the first minute of the experiment, then peaked at 8 cm^3. This result supports the conclusion that the SMP concentration plays a significant role in sealing efficiency, especially with the larger fractures.

3.3. Numerical Simulation

There are different proposed models in the literature that have contradictory scenarios regarding the particle bridging locations. The two major proposed mechanisms for wellbore strengthening applications are the stress cage and fracture closure stress enhancement (Alberty, 2004; Aston et al., 2004; Dupriest, 2005). The stress cage concept suggests that a fracture is propped open, and the particles bridge near the mouth to increases the hoop stress. On the other hand, the concept of fracture closure stress suggests the bridging process occurs inside the fracture at a distance from the mouth. In addition, fracture propagation resistance model also suggests that the fracture seal occurs near the fracture tip to raise the effective propagation pressure (van Oort and Razavi, 2014). Lavrov (2016) pointed out that there might be more than one mechanism at work instead of just one. Although our model is applicable to natural fractures, the simulation results still provide insights on the bridging process.

According to our simulation results in Figure 9, the initial bridging location occurs in the vicinity of the fracture entrance, where most of the LCM particle collisions take place. Once an initial bridge forms, it becomes a body of restriction or a plug to permit a less flow volume. The pressure propagation caused by high inlet pressure is also stopped by the bridged particles, thus resulting in a large pressure drop across the

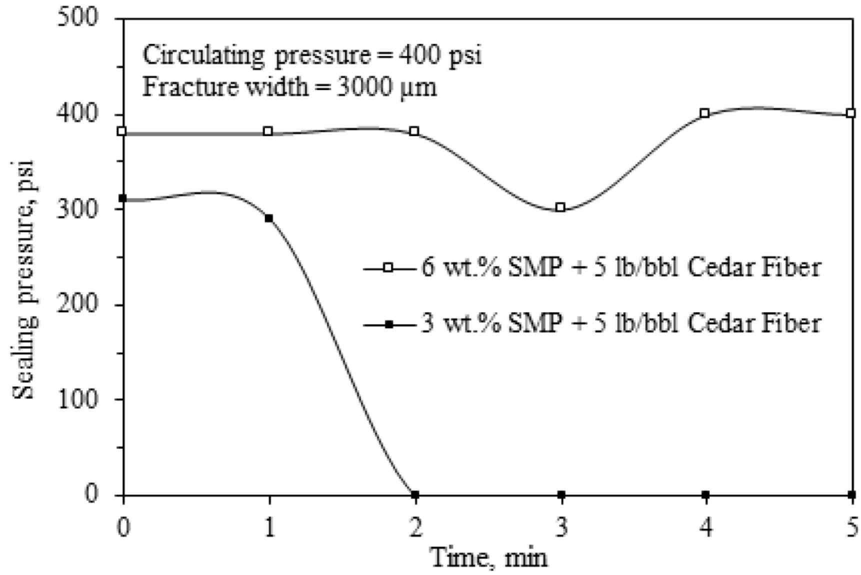

Fig. 7. Sealing pressure from dynamic LCM testing experiments with 3,000μm fracture with two different SMP concentrations.

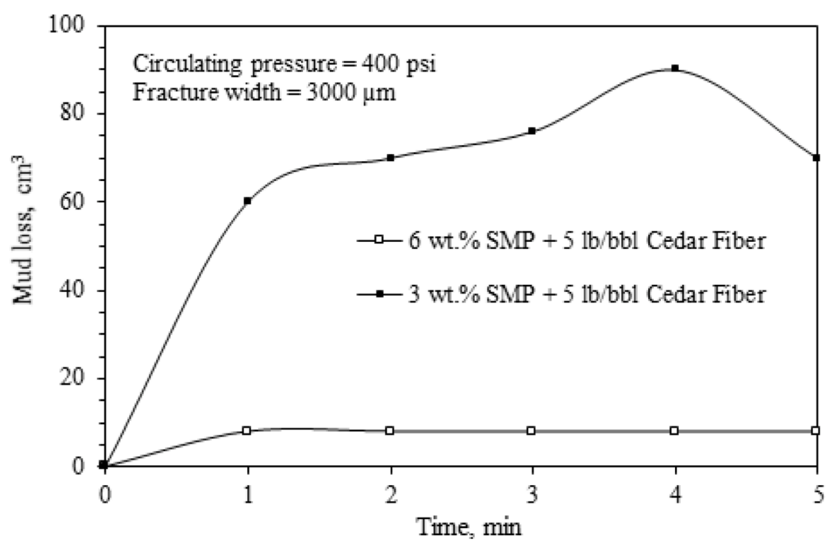

Fig. 8. Mud loss from dynamic LCM testing experiments with 3,000μm fracture with two different SMP concentrations.

bridge. The bridge also moves closer towards the fracture outlet due to higher stress applied on the upstream particles than the downstream side. As shown in Figure. 9, snapshots of particles inside the wellbore geometry system exhibit the gradual progression of the plug towards the fracture outlet. The pressure contour maps indicate that the high pressure is stopped at the fracture entrance and not able to propagate further because of the hydraulic barrier created by the LCM particles.

In addition, bridged particles exhibit compressive forces against neighboring particles. The overall force structure is mapped in Figure 10, where the LCMs have accumulated tightly inside the fracture. The integrity of the force network is maintained when sufficient sliding friction (both particle-particle and particle-wall), rolling friction, and cohesive energy are provided. The cohesive nature of LCMs plays an important role in sealing large fracture as they form large clusters in a narrow channel.

In fact, we have also observed from cases with different LCM mixtures that a plug may not form. The reason is attributed to fluid viscosity, frictions (particle-particle and particle-wall), particle sphericity, and proper particle size distribution. Illustrated in Figure. 11, there are two common bridging scenarios. In the first scenario as shown in Figure. 11**a**, the particles accumulate on the surface of the cylindrical pipe where it connects to the fracture. The fracture aperture is too small for particulate matters to flow in. This is mostly due to a high concentration of large particles in the PSD design. On the other hand, if there is a high concentration of small particles in the PSD and not enough large particles, they always end up stacking on the lower part of the fracture entrance as seen in Figure. 11**b**. This results in a narrow region with high fluid velocity where most particles would be entering and flushed out to the outlet.

The fluid loss rate measured at the fracture outlet may indicate whether the fracture is sealed. Three cases of LCM mixtures with different SMP concentrations were tested. These concentrations include 10%, 15%, and 20% SMP by volume. When using an LCM mixture with 10% SMP, the system exhibits particle accumulation on the bottom of the fracture entrance, similar to that of Figure 11**b**. However, a complete seal can be established when the SMP concentration is increased to above 15%. Thus, we utilized dimensionless parameters to analyze whether loss prevention is successful. The dimensionless flowrate is the ratio of fluid loss rate at the fracture outlet to its initial loss rate while the dimensionless time is the ratio of passed fluid volume to fracture

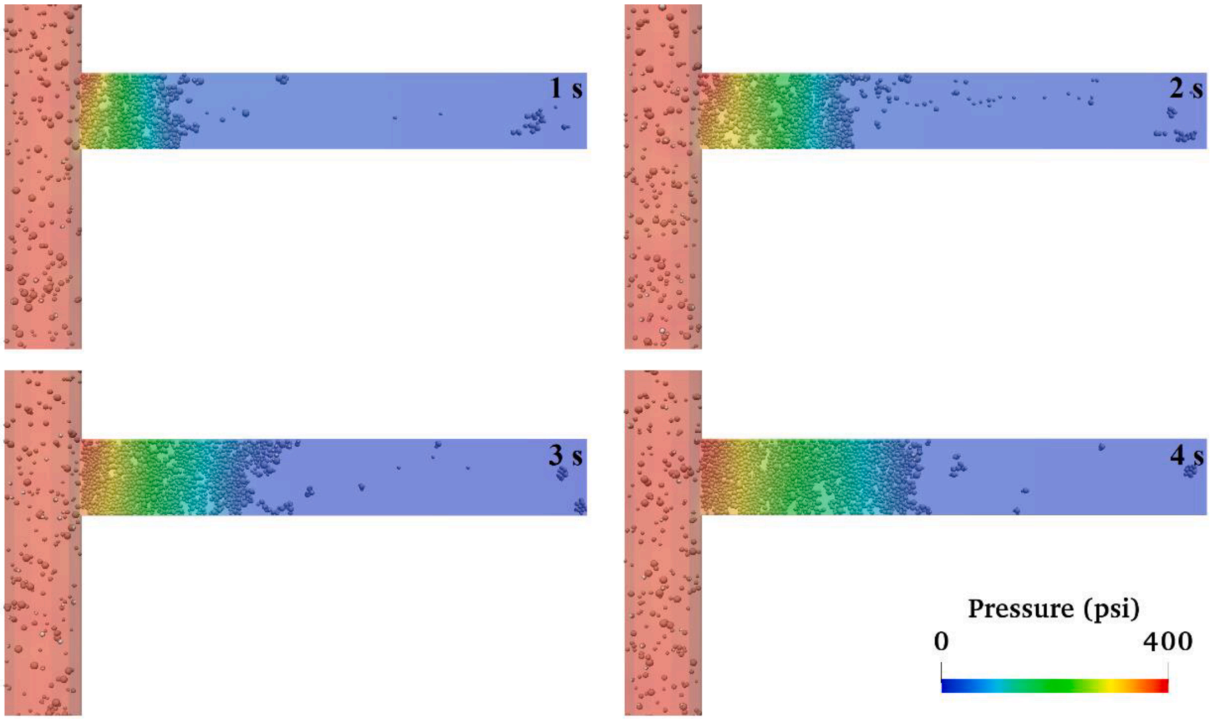

Fig. 9. Snapshots of the plug form by the LCMs in the wellbore geometry system.

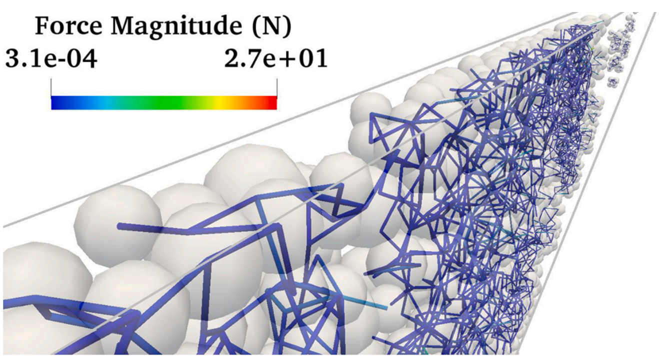

Fig. 10. Bridged particles with the network of compressive forces. The wellbore is located at the left-hand side of the pictures.

volume. Initially, there are no particles in the wellbore system. The quick spike in Figure 12 is due to system being filled with particles. The loss rate slowly decreases once the LCM particles accumulate and establish a complete seal. A plug can be found in both mixtures of 15% and 20% SMP, which is reflected by their decrease in the loss rate to around 2 in Figure 12. On the other hand, an establishment of a plug was not formed from the LCM mixture of 10% SMP.

In loss diagnostics, our wellbore geometry system can be identified as fluid loss into a natural fracture. The shape of loss rate versus time is unique for different types of formation. For example, an onset loss may be quickly observed due to mud flowing into a natural fracture. The high loss rate slowly decreases once a plug forms inside the fracture and lowers its permeability. The loss typology in Figure 12 matches with field measurements (Beda and Carugo, 2001).

3.4. Remarks on Numerical System and the Flow Loop

The CFD-DEM numerical simulation can be a useful supplementary tool to analyze fracture sealing efficiency. Figure 13 shows the mud loss vs dimensionless time for both numerical and the laboratory results. The dimensionless time is to help put both laboratory and simulation results on the same scale. The CFD-DEM simulation consumes a large

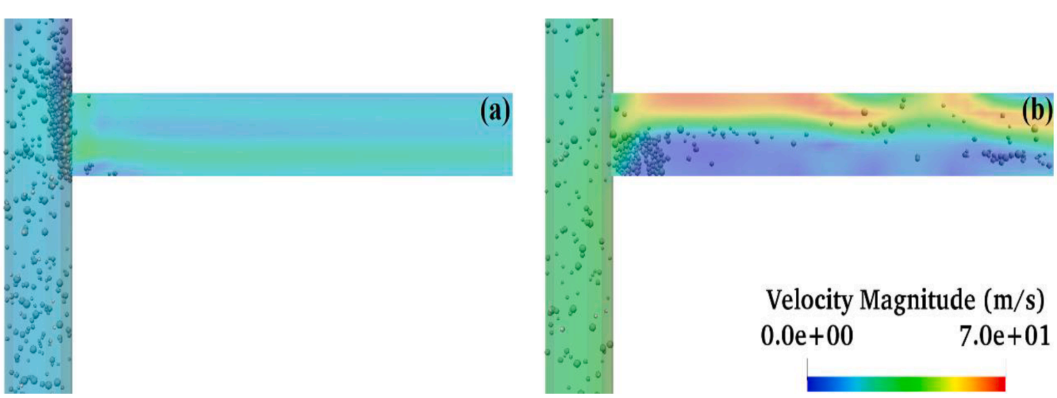

Fig. 11. Two common locations where LCMs may be located. (a) Particles accumulate at the pipe surface, unable to flow into the fracture. (b) The LCMs stack on the lower part of the fracture inlet.

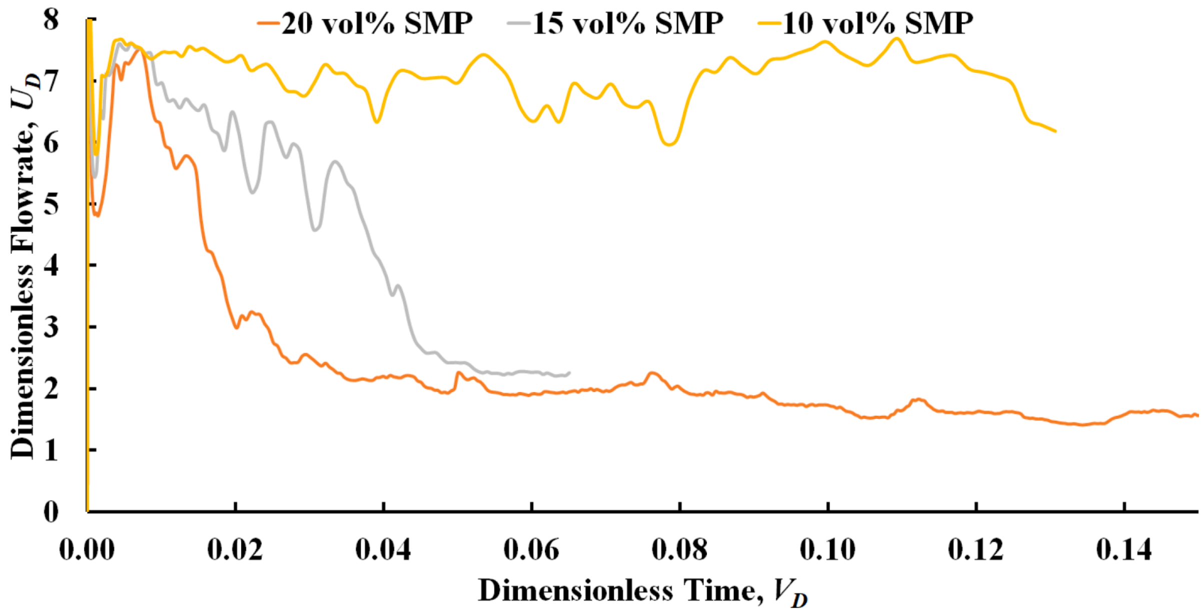

Fig. 12. Fluid rate comparison between three numerical cases including 10%, 15%, and 20% SMP by volume.

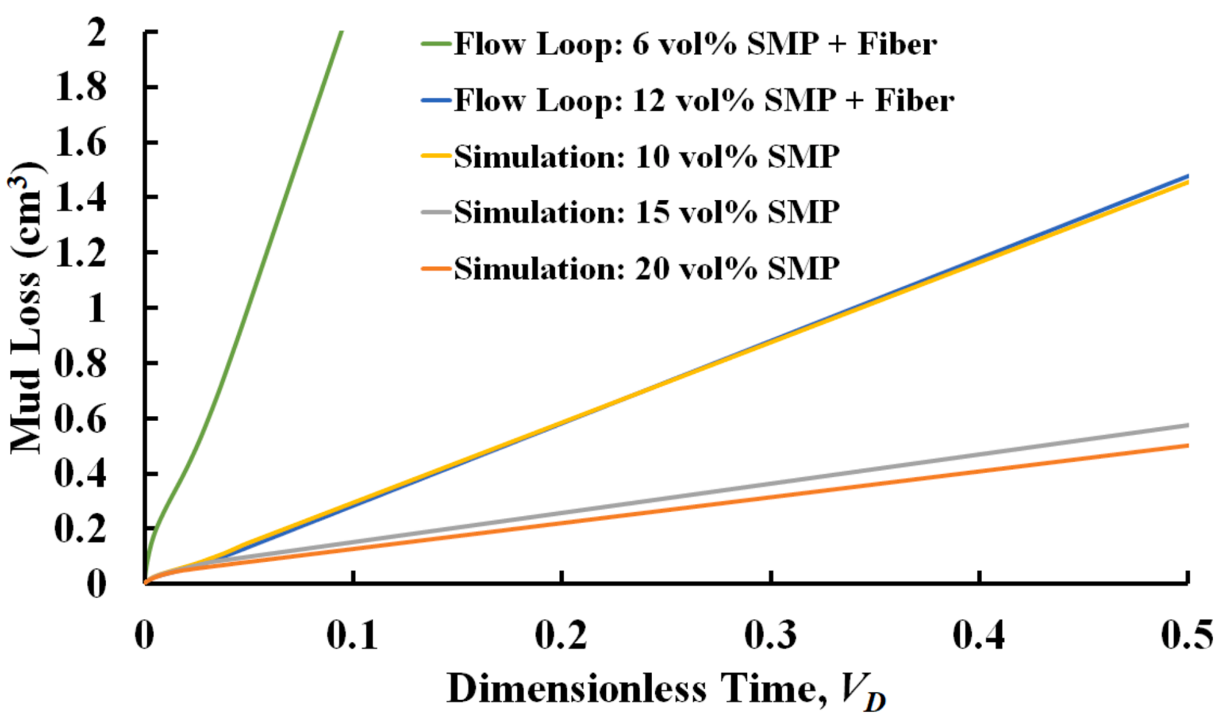

Fig. 13. Mud loss comparison between the numerical and laboratory results.

computational power, and therefore cannot represent the whole laboratory scenario. However, the first 60-seconds can still be represented. The 3 and 6 wt% SMP are equivalent to 6 and 12 vol% SMP. Fracture sealing was not successful for a mixture of 6 vol% SMP with fiber. The best case in minimizing mud loss indicates a mixture of 20 vol% SMP, which is slightly better than a mixture of 15 vol% SMP. The recorded mud loss is similar for both simulated 10 vol% SMP and 12 vol% SMP with fiber. This is not to say fibers are effectless. Fibrous materials are used to help initiate bridging. The fibers are entangled when flowing inside a permeable channel. A net-like structure is the result of the fiber entanglement which reduces the size of openings and help capture incoming granular particles. Due to simulation constraint, only granular LCMs and SMP were modelled. In fact, the laboratory conditions are set as close as possible to the simulation conditions. Although not completely the same, the rolling friction and cohesive energy are imposed on LCMs in the CFD-DEM to incorporate the shape effect and mimic the cohesive nature of SMP in high temperature environment. These parameters may be carefully tuned using a test such as the angle of repose test (Roessler and Katterfeld, 2019).

4. Conclusion

Lost circulation prevention and remediation require the use of bridging particles, where the particles bridge and seal any permeable path in the formation. However, large fractures are not sealable by conventional LCMs due to potential clogging of downhole equipment by using large bridging particles. These large fractures often exist in high-temperature geological locations such as geothermal wells. This very often causes traditional LCMs such as calcium carbonates to degrade. The sealing capability of SMP have been evaluated both in the laboratory setup and in numerical simulations. A wellbore geometry system with large fracture (3 mm) was created to test the sealing ability of LCMs made of SMP in the lab. The key findings are documented as the following:

- The SMP particles looks very promising for sealing large fractures as they utilize the formation temperature as the trigger mechanism.
- The coupled CFD-DEM simulation has been adapted and validated for simulating the plugging process by SMP particles.
- The simulation shows that a plug can be formed when the SMP concentration reaches 15% by volume. Increasing the concentration further to 20% would have slight reduction in fluid loss. The outcomes are in agreement with our laboratory observations.
- The CFD-DEM simulation can assist the laboratory work as the LCM recipes may be modified and adjusted accordingly without the need of running an expensive experiment. The wellbore geometry system was used for the first time in such simulations to mimic the dynamic flow loop system used in the laboratory.
- The plugging location as well as the integrity of the plugged LCMs can be examined by their compressive forces exerted on each other in numerical simulations.

Author Statement

Lu Lee: Software, Writing original draft, validation
Musaab Magzoub: Conducting experiment, Writing a part of the draft
Arash Dahi Taleghani: Advising, conceptualization, reviewing and revising the manuscript
Saeed Salehi: Advising, funding

Declaration of Competing Interest

None.

Acknowledgement

This research was funded by the U.S. Department of Energy's Office of Energy Efficiency and Renewable Energy (EERE) under the Geothermal Program Office, award number DE EE0008602.

References

Abrams, A., 1977. Mud design to minimize rock impairment due to particle invasion. J. Petrol. Tech. 29 (5), 586–592. https://doi.org/10.2118/5713-PA. SPE-5713-PA.
Ai, J., Chen, J.-F., Rotter, J.M., Ooi, J.Y., 2011. Assessment of rolling resistance models in discrete element simulations. Powder Technol. 206, 269–282. https://doi.org/10.1016/j.powtec.2010.09.030.
Alberty, M.W., McLean, M.R., 2004. A physical model for stress cages. Paper presented at the SPE Annual Technical Conference and Exhibition 26–29. https://doi.org/10.2118/90493-MS. Houston, Texas, USA, SeptemberSPE-90493-MS.
Alsaba, M., Nygaard, R., Hareland, G., et al., 2014. In: , pp. 15–16. Houston, Texas, USA, AprilAADE-14-FTCE-25.
Alsaba, M., Al Dushaishi, M.F., Nygaard, R., et al., 2017. Updated criterion to select particle size distribution of lost circulation materials for an effective fracture sealing. J. Pet. Sci. Eng. 149, 641–648. https://doi.org/10.1016/j.petrol.2016.10.027.
Amani, M., Al-Jubouri, M., Shadravan, A., 2012. Comparative study of using oil-based mud versus water-based mud in HPHT fields. Adv. Petrol. Explor. Dev. 4 (2), 18–27. https://doi.org/10.3968/j.aped.1925543820120402.987.
Anderson, T.B., Jackson, R., 1967. Fluid Mechanical Description of Fluidized Beds. Equations of Motion. Eq. Mot. Indust. Eng. Chem. Fundament. 6 (4), 527–539. https://doi.org/10.1021/i160024a007.
Aston, M.S., Alberty, M.W., McLean, M.R., et al., 2004. Drilling fluids for wellbore strengthening. Paper Presented at the IADC/SPE Drilling Conference. https://doi.org/10.2118/87130-MS. Dallas, Texas, USA, 2–4 MarchSPE-87130-MS.
Avci, E., Mert, B.A., 2019. The rheology and performance of geothermal spring water-based drilling fluids. GeoFluids. https://doi.org/10.1155/2019/3786293, 2019:
Baret, J.-F., Daccord, G., Yearwood, J., 1990. Cement/Formation interactions. Well Cementing. Elsevier Science Publishing.
Beda, G., Carugo, C., 2001. Use of mud microloss analysis while drilling to improve the formation evaluation in fractured reservoir. In: Paper presented at the SPE Annual Technical Conference and Exhibition, New Orleans, Louisiana, USA, September 30–October 3. SPE-71737-MS. https://doi.org/10.2118/71737-MS.
Candelier, F., Angilella, J.R., Souhar, M., 2004. On the effect of the Boussinesq-Basset force on the radial migration of stokes particle in a vortex. Phys. Fluids 16, 1765–1776. https://doi.org/10.1063/1.1689970.
Chellappah, K., Aston, M.S., 2012. A new outlook on the ideal packing theory for bridging solids. In: Paper presented at the SPE International Symposium and Exhibition on Formation Damage Control, Lafayette, Louisiana, USA, February 15–17. SPE-151636-MS. https://doi.org/10.2118/151636-MS.
Cundall, P.A., Strack, O.D.L., 1979. A discrete numerical model for granular assemblies. Géotechnique 29 (1), 47–65. https://doi.org/10.1680/geot.1979.29.1.47.
Di Felice, R., 1994. The voidage function for fluid-particle interaction systems. Int. J. Multiphase Flow 20 (1), 153–159. https://doi.org/10.1016/0301-9322(94)90011-6.
Dick, M.A., Heinz, T.J., Svoboda, C.F., et al., 2000. In: Optimizing the Selection of Bridging Particles for Reservoir Drilling Fluids. Paper presented at the SPE Internation Symposium on Formation Damage Control, Lafayette, Louisiana, USA, February 23–24. SPE-58793-MS. https://doi.org/10.2118/58793-MS.
Dupriest, F.E., 2005. In: Fracture Closure Stress (FCS) and Lost Returns Practices. Paper presented at the SPE/IADC Drilling Conference, Amsterdam, the Netherlands, February 23–25. SPE-92192-MS. https://doi.org/10.2118/92192-MS.
Fan, J., Li, G., 2018. High enthalpy storage thermoset network with giant stress and energy output in rubbery state. Nat. Commun. 9 (1), 642. https://doi.org/10.1038/s41467-018-03094-2.
Finger, J., Blankenship, D., 2012. Handbook of best practices for geothermal drilling. Sandia Rep.
Fourche, G., 1995. An overview of the basic aspects of polymer adhesion. Part I: Fundamentals. Polym. Eng. Sci. 35 (12), 957–967. https://doi.org/10.1002/pen.760351202.
Galindo, K.A., Zha, W., Zhou, H., et al., 2015. High temperature, high performance water-based drilling fluid for extreme high temperatrue wells. In: Paper presented at the SPE International Symposium on Oilfield Chemistry, The Woodlands,Texas, USA, April 13–15. SPE-173773-MS. https://doi.org/10.2118/173773-MS.
Gatlin, C., Nemir, C.E., 1961. Some effects of size distribution on particle bridging in lost circulation and filtration tests. J. Petrol. Tech. 13 (6) https://doi.org/10.2118/1652-G-PA, 575–578. SPE-1652-G-PA.
Gidaspow, D., 1994. Transport equations. Multiphase Flow and Fluidization. Academic Press.
Goniva, C., Kloss, C., Deen, N.G., et al., 2012. Influence of rolling friction on single spout fluidized bed simulation. Particuology 10, 582–591. https://doi.org/10.1016/j.partic.2012.05.002.
Hertz, H., 1882. Ueber die Berührung fester elastischer Körper. J. Reine Angew. Math. 92, 156–171. https://doi.org/10.1515/crll.1882.92.156.
Kloss, C., Goniva, C., Hager, A., et al., 2012. Models, algorithms and validation for opensource DEM and CFD-DEM. Progr. Comput. Fluid Dyn. 12 (2/3), 140–152. https://doi.org/10.1504/PCFD.2012.047457.
Johnson, K.L., Kendall, K., Roberts, A.D., 1971. Surface energy and the contact of elastic solids. Proc. R. Soc. Lond. Series A 324, 301–313. https://doi.org/10.1098/rspa.1971.0141.
Lavrov, A., 2016. Lost Circulation: Mechanisms and Solutions. Gulf Professional Publishing.
Lee, L., Dahi Taleghani, A., 2020. The effect of particle size distribution of granular LCM on fracture sealing capability. In: Paper presented at the SPE Annual Technical Conference and Exhibition, October 26–29, virtual. SPE-201668-MS. https://doi.org/10.2118/201668-MS.
Li, G., 2014. Thermoset Shape Memory Polymer and Its Syntactic Foam. Self-Healing Composites: Shape Memory Polymer Based Structures. John Wley & Sons.
Magzoub, M., Anyaezu, T., Salehi, S., et al., 2021. Evaluating sealability of blended smart polymer and fiber additive for geothermal drilling with the effect of fracture opening size. J. Pet. Sci. Eng. 206, 108998 https://doi.org/10.1016/j.petrol.2021.108998.
Mansour, A., Dahi Taleghani, A., Salehi, S., et al., 2018. Smart lost circulation materials for productive zones. J. Petrol. Explor. Prod. Tech. 9, 281–296. https://doi.org/10.1007/s13202-018-0458-z.
Maruyama, Y., 2011. Study on the physical mechanism of the magnus effect. Trans. Jpn. Soc. Aeronaut. Space Sci. 54, 173–181. https://doi.org/10.2322/tjsass.54.173.
Razavi, O., Vajargah, A.K., van Oort, E., 2015. How to effectively strengthen wellbores in narrow drilling margin wells: an experimental investigation. In: Paper presented at the SPE Annual Technical Conference and Exhibition, Houston, Texas, USA, September 28–30. SPE-174976-MS. https://doi.org/10.2118/174976-MS.
Razavi, O., Vajargah, A.K., van Oort, E., et al., 2016. Optimum particle size distribution design for lost circulation control and wellbore strengthening. J. Nat. Gas Sci. Eng. 35, 836–850. https://doi.org/10.1016/j.jngse.2016.08.038.
Roessler, T., Katterfeld, A., 2019. DEM parameter calibration of cohesive bulk materials using a simple angle of repose test. Particuology 45, 105–115. https://doi.org/10.1016/j.partic.2018.08.005.
Rumpf, H.C.H., Gupte, A.R., 1971. Einflüsse der Porosität und Korngrößenverteilung im Widerstandsgesetz der Porenströmung. Chem. Ing. Tech. 43, 367–375. https://doi.org/10.1002/cite.330430610.
Saffman, P.G., 1964. The lift on a small sphere in a slow shear flow. J. Fluid Mech. 22 (2), 385–400. https://doi.org/10.1017/S0022112065000824.

Tabatabaei, M., Dahi Taleghani, A., 2021. Smart lost circulation materials to seal large fractures. In: Paper presented at the SPE Annual Technical Conference and Exhibition, Dubai, UAE, September 21–23. SPE-205873-MS. https://doi.org/10.2118/205873-MS.

Tabatabaei, M., Dahi Taleghani, A., Li, G., et al., 2021. In: Shape Memory Polymers as Lost Circulation Materials for Sealing Wide-Opened Natural Fractures. SPE Drilling and Completion: 1–12. SPE-205514-PA. https://doi.org/10.2118/205514-PA.

van Oort, E., Razavi, S.O., 2014. In: Wellbore Strengthening and Casing Smear: The Common Underlying Mechanism. Paper presented at the IADC/SPE Drilling Conference and Exhibition, Fort Worth, Texas, USA, March 4–6. SPE-168041-MS. https://doi.org/10.2118/168041-MS.

Vickers, S., Cowie, M., Jones, T., et al., 2006. In: A New Methodology That Surpasses Current Bridging Theories to Efficiently Seal A Varied Pore Throat Distribution as Found in Natural Resrvoir Formations. Paper presented at the AADE Drilling Fluids Technical Conference, April 11–12, Houston, Texas, USA. AADE-06-DF-HO-16.

Wang, G., Huang, Y., Xu, S., 2019. Laboratory investigation of the selection criteria for the particle size distribtuion of granular lost circulation materials in naturally fractured reservoirs. J. Nat. Gas Sci. Eng. 71, 103000 https://doi.org/10.1016/j.jngse.2019.103000.

Whitfill, D.L., Fang, C.C., Miller, M., 2011. In: Lost Circulation Material Formulation and Method of Use. US Patent No. 8,043,997 B2.

Zhou, Z.Y., Kuang, S.B., Chu, K.W., et al., 2010. Discrete particle simulation of particle-fluid flow: model formulations and their applicability. J. Fluid Mech. 661, 482–510. https://doi.org/10.1017/S002211201000306X.